

# Area-Selective Lift-Off Mechanism Based on Dual-Triggered Interfacial Adhesion Switching: Highly Facile Fabrication of Flexible Nanomesh Electrode

Seunghye Yu,<sup>†,⊥</sup> Hyeuk Jin Han,<sup>†,⊥</sup> Jong Min Kim,<sup>†</sup> Soonmin Yim,<sup>†</sup> Dong Min Sim,<sup>†</sup> Hunhee Lim,<sup>†</sup> Jung Hye Lee,<sup>†</sup> Woon Ik Park,<sup>‡</sup> Jae Hong Park,<sup>§</sup> Kwang Ho Kim,<sup>\*,‡,§,⊥</sup> and Yeon Sik Jung<sup>\*,†,§,⊥</sup>

<sup>†</sup>Department of Materials Science and Engineering, Korea Advanced Institute of Science and Technology (KAIST), 291 Daehak-ro, Yuseong-gu, Daejeon 34141, Republic of Korea

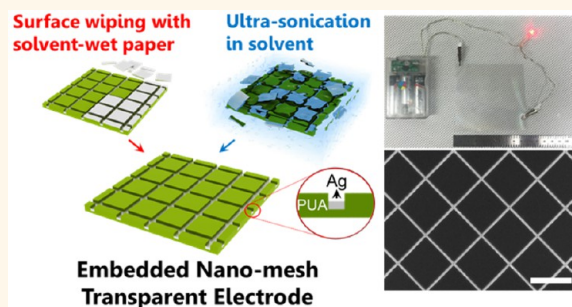
<sup>‡</sup>Global Frontier R&D Center for Hybrid Interface Materials (HIM), Pusandaehak-ro 63beon-gil, Geumjeong-gu, Busan 46241, Republic of Korea

<sup>§</sup>Division of Nano-Convergence Technology, Korea National NanoFab Center, 291 Daehak-ro, Daejeon 34141, Republic of Korea

## Supporting Information

**ABSTRACT:** With the recent emergence of flexible and wearable optoelectronic devices, the achievement of sufficient bendability and stretchability of transparent and conducting electrodes (TCEs) has become an important requirement. Although metal-mesh-based structures have been investigated for TCEs because of their excellent performances, the fabrication of mesh or grid structures with a submicron line width is still complex due to the requirements of laborious lithography and pattern transfer steps. Here, we introduce an extremely facile fabrication technique for metal patterns embedded in a flexible substrate based on submicron replication and an area-selective delamination (ASD) pattern. The high-yield, area-specific lift-off process is based on the principle of solvent-assisted delamination of deposited metal thin films and a mechanical triggering effect by soft wiping or ultrasonication. Our fabrication process is very simple, convenient, and cost-effective in that it does not require any lithography/etching steps or sophisticated facilities. Moreover, their outstanding optical and electrical properties (e.g., sheet resistances of  $0.43 \, \Omega \, \text{sq}^{-1}$  at 94% transmittance), which are markedly superior to those of other flexible TCEs, are demonstrated. Furthermore, there is no significant change of resistance over 1000 repeated bending cycles, with a bending radius of 5 mm, and immersion in various solvents such as salt water and organic solvents. Finally, we demonstrate high-performance transparent heaters and flexible touch panels fabricated using the nanomesh electrode, confirming the long-range electrical conduction and reliability of the electrode.

**KEYWORDS:** interfacial adhesion switching, area-selective lift-off, solvent, mechanical stimulus, transparent conductor, metal mesh, embedded structure



Emerging flexible optoelectronic devices such as flexible solar cells,<sup>1</sup> touch panels,<sup>2,3</sup> and displays<sup>4</sup> require transparent conducting electrodes (TCEs) with sufficient mechanical flexibility in addition to high conductivity and high optical transparency. In accordance with these requirements, conventional transparent conductive oxides (TCOs) such as indium tin oxide (ITO) should be replaced with alternative flexible transparent conductors due to the brittleness of the oxide materials.<sup>5,6</sup> Furthermore, the optical transmittance of TCO films significantly decreases with an increase of film thickness for low sheet resistance,<sup>7</sup> which prevents its use for an extremely low-resistance TCE. Thus, new material systems such

as metal nanowire networks,<sup>1,8–10</sup> carbon-based materials,<sup>4,11,12</sup> conducting polymers,<sup>13</sup> and mesh or grid patterned metals<sup>14–19</sup> have been actively investigated to achieve both high flexibility and good optoelectronic performance.

Among them, metal-based electrodes are leading candidates because of their excellent electrical conductivity, flexibility, and cost-effectiveness. Diverse approaches to realize metal-based

**Received:** January 11, 2017

**Accepted:** February 28, 2017

**Published:** February 28, 2017

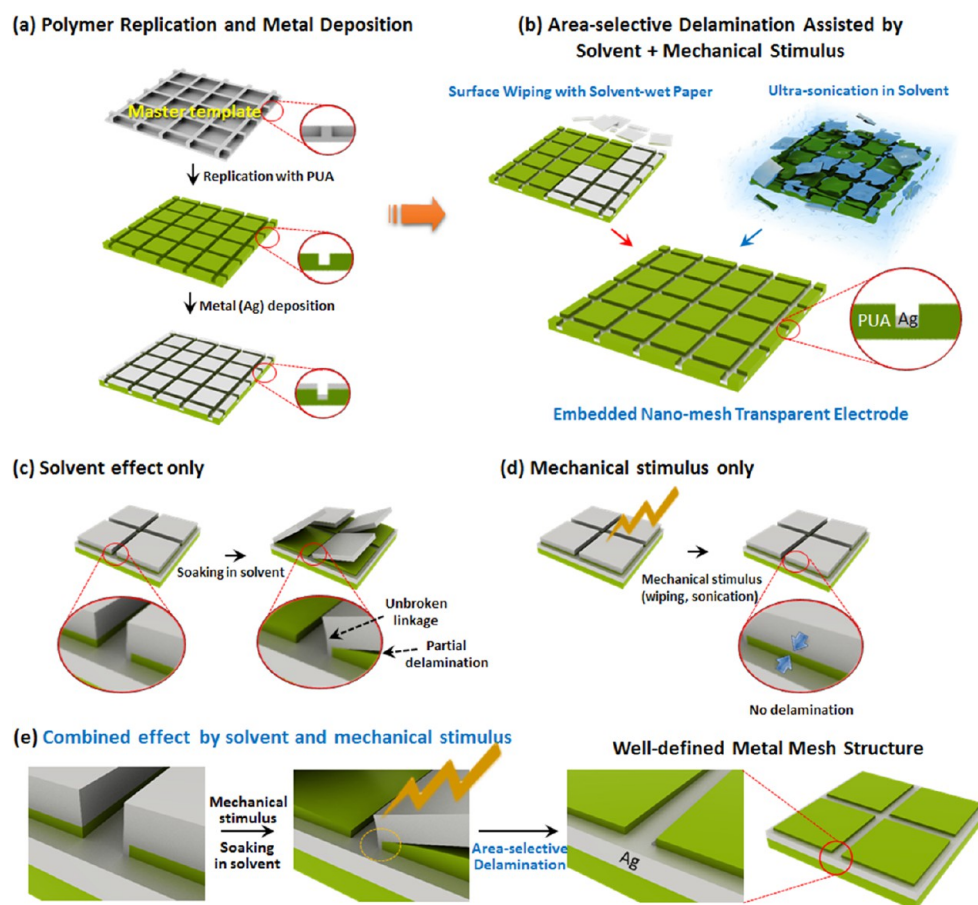


**Figure 1.** Schematic of the fabrication of the embedded metal-nanomesh transparent electrode based on a solvent-assisted area-selective delamination principle. The whole procedure is composed of two subprocesses. (a) The Si master template is prepared using photolithography and dry-etching of the Si wafer, followed by replication of the master using PUA and evaporative deposition of a metal such as Ag on the PUA replica/PET substrate. (b) For the selective removal of metal patterns from the mesa regions, solvent-assisted delamination techniques were developed. The simultaneous application of the solvent that swells the PUA replica and a mechanical stimulus can induce preferential detachment of the metal structures only from the mesa region. Two types of area-selective delamination, (1) soft wiping with a solvent-soaked paper wiper and (2) ultrasonication in a solvent, are demonstrated. (c) When there is only a solvent effect, Ag square plates cannot be perfectly delaminated because Ag square plates and embedded metal parts are connected through the sidewall. (d) When only mechanical stimulus is applied without using a proper solvent, Ag square plates cannot be detached due to the strong interfacial interaction. (e) Well-defined metal-mesh structure can be fabricated by the synergistic combination of solvent-assisted adhesion switching and external mechanical stimulus.

composites have been studied thus far. For example, electrospinning of silver nanowires can provide low sheet resistance, high optical transmittance, and excellent flexibility.<sup>8,20,21</sup> However, this method typically requires an additional welding process using heat, mechanical pressure, or a light-exposure process to reduce the contact junction resistance between silver nanowires.<sup>8,22,23</sup> Also, these procedures can degrade flexible polymer substrates such as polyethylene terephthalate (PET) and, therefore, may demand more expensive flexible substrates with better thermal stability, such as colorless polyimide.<sup>24</sup> In addition, multilayer silver nanowires can significantly scatter incident light, which is associated with optical haze.<sup>25</sup>

On the other hand, metal-mesh-patterned electrodes are entirely interconnected without a contact junction, and thus these electrodes **innately** have a high electrical conductivity. Moreover, high-quality polycrystal structures can be obtained because metal meshes are generally fabricated using high-purity deposition processes such as evaporative deposition and electrodeposition.<sup>16,18,19</sup> In addition, compared to nanowire films with random networks, metal-mesh patterns are regularly

arranged over the entire electrode area, thus presenting superior uniformity and reliability.<sup>26</sup> This is because, even if local open-circuit points exist, there are alternative routes for electrical conduction. Moreover, the small line widths (typically micrometer to sub-micrometer range) of the mesh geometry and the natural ductility of metallic materials provide outstanding mechanical flexibility.<sup>16,19</sup> Furthermore, geometric factors such as line width, height, and morphology can be independently controlled, and as a result, the electrical properties can be widely tuned.<sup>19,27</sup>

For these reasons, metal-mesh-patterned electrodes have received a great deal of attention and extensive research has been carried out. Recently, Li and co-workers reported a high-performance flexible transparent electrode with an embedded metal mesh that offers a high figure-of-merit value and superior bendability compared to that of conventional non-embedded metal meshes.<sup>19</sup> This is attributed to the sidewalls surrounding the embedded mesh structures providing better adhesion with the substrate. **An embedded pattern has superior oxidation stability because its exposed area is smaller than that of**



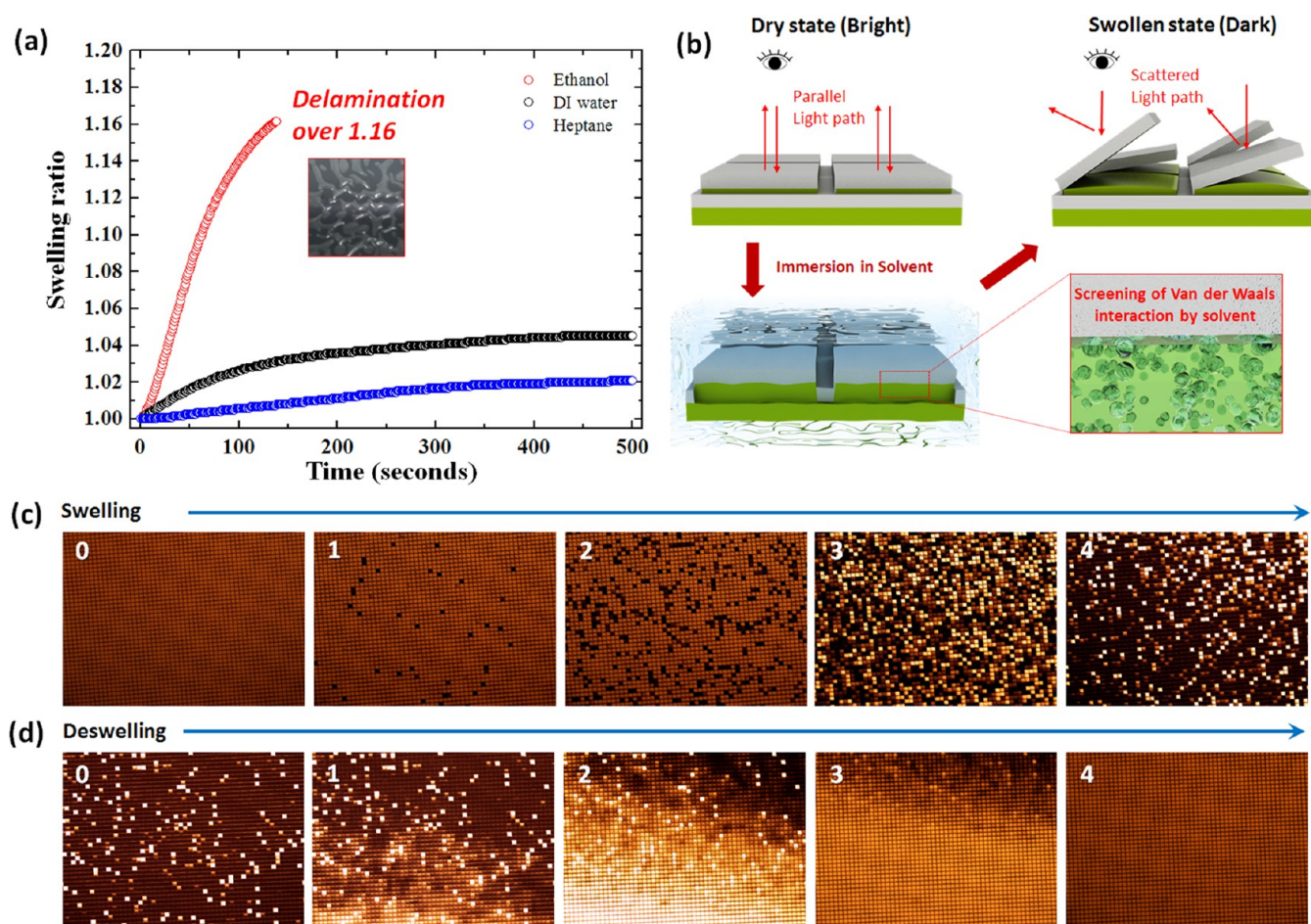


**Figure 2.** Solvent-assisted delamination between metal and PUA. (a) Swelling ratio of PUA substrates under the saturated vapor of water, ethanol, and heptane. PUA was the most significantly swollen by ethanol among the evaluated solvents. (b) Schematic of solvent-swollen Ag/PUA replica. Normal reflection and off-axis reflection on the surface of Ag can explain the change of the images of the samples. (c) *In situ* optical microscope images of the Ag-deposited PUA replica substrate in ethanol (number: time sequence). The fraction of dark parts increases due to the oblique angle reflection from the Ag surface, which is caused by the swelling of PUA in ethanol and resultant (partial) delamination of Ag square structures on the mesa regions of PUA. The brightness of the images was automatically adjusted. (d) Change of the image of sample (c) after removing it from the ethanol bath. With drying of the sample, the dark spots returned to bright spots, suggesting that the Ag squares were not completely detached from the PUA surface despite the immersion in ethanol.

**conventional structures.** In addition, an **electrohydrodynamic** (EHD) printing method was demonstrated by Poulikakos and co-workers, and they achieved nanoscale resolution and three-dimensional structure formation capabilities for high-aspect-ratio metal grid electrodes.<sup>28</sup> Despite these efforts and achievements, however, it remains a challenge to simultaneously overcome multiple issues such as further simplification of the manufacturing process by eliminating photolithography or etching steps, reduction of facility cost, increase of throughput, and improvement of electrical and optical performance.

Here, we introduce a highly facile method for the fabrication of high-performance metal-nanomesh flexible transparent electrodes with extremely low resistance and high transmittance. We combined a conventional nanomolding replication technique and **area-selective delamination** (ASD) nanopatterning driven by the interfacial adhesion control mechanism, which is based on solvent injection and mechanical stimulus for locally controlled, uniform delamination of metal structures. Our strategy includes replication of master templates, solvent-induced adhesion switching of the metal/polymer interface, and area-selective lift-off of metal films from

the mesa region of the replicas, which is triggered by a mechanical stimulus. The replicas with submicron topographic structures were formed using **polyurethane acrylate** (PUA), which can replicate a wide range of mesh width and height and has clear optical transparency with a thin layer.<sup>29</sup> Moreover, owing to the stability of UV-cross-linked PUA in various solvents, it is adequate for an ASD process. This process does not require a sophisticated patterning machine or cumbersome metal etching processes and satisfies all of the above-mentioned requirements such as low processing cost and simple fabrication while maximizing the optical and electrical performance. We also demonstrate the mechanical stability of the embedded metal-mesh structure over 1000 bending cycles and its chemical stability in harsh environments such as an organic solvent and salt water.

## RESULTS AND DISCUSSION

The fabrication process for the embedded-type metal-nanomesh-patterned flexible transparent electrodes is schematically illustrated in Figure 1. First, PUA was drop-cast onto the mesh-patterned Si master mold to inversely replicate the surface geometry (Figure 1a). We used two types of PUA with different

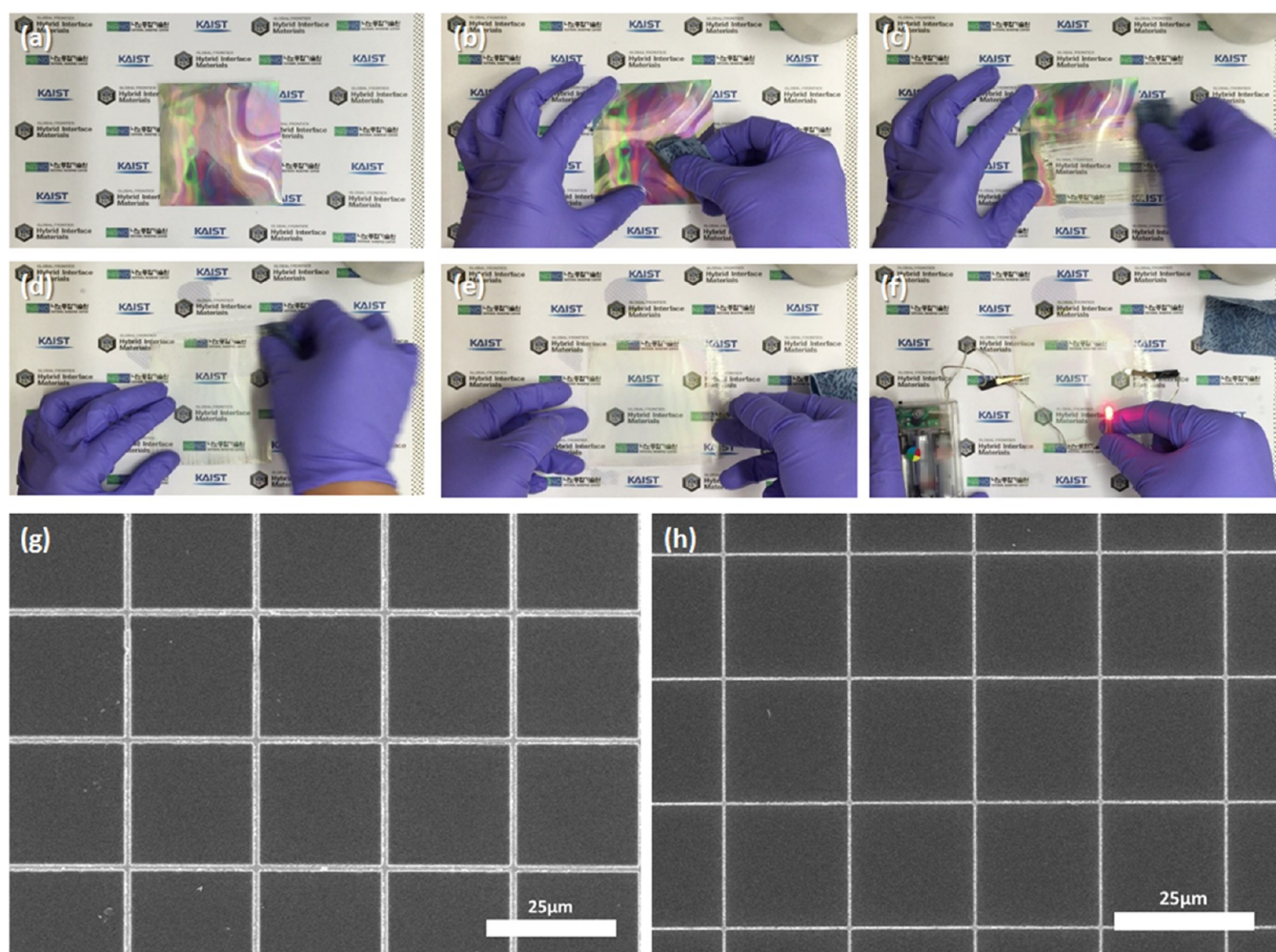


**Figure 3.** Fabrication of metal-mesh electrode by soft wiping ASD patterning. (a–f) Optical images of wiping delamination process; used with permission, the background is the logos of Korea Advanced Institute of Science and Technology (KAIST), National NanoFab Center (NNFC), and Global Frontier Hybrid Interface Materials (HIM). Rubbing of the Ag/PUA replica/PET with an ethanol-soaked paper towel selectively removes the Ag square structures. (g,h) SEM images of embedded-type metal-mesh flexible transparent electrodes by wiping-based ASD process with a period of 26  $\mu\text{m}$  and line widths of 900 and 400 nm.

swelling behavior in ethanol (see the [Experimental Section](#) for details). In order to obtain sufficient flexibility and durability of the final electrode, PET was used as a supporting substrate attached on PUA, and the PUA replica/PET was cured with UV light irradiation *via* cross-linking. The submicron-wide mesh structures were successfully replicated due to the good molding resolution of PUA, even below 100 nm.<sup>30</sup> Ag was then deposited on the surface of the PUA replicas *via* thermal evaporation. During the process of evaporative deposition, Ag fills the trenches with an inverse-mesh structure and is also deposited on the square-shaped mesa region (bottom of [Figure 1a](#)). The deposition angle and the distance between the source and the substrate were optimized to minimize the thickness of the films deposited on the sidewalls of the PUA patterns. As a result, Ag deposited on the PUA replica can be divided into two parts—(1) the embedded nanomesh in the trench region and (2) the square plate patterns on the mesa region—and **these two regions are weakly connected to each other *via* the thin layer coated on the sidewall.**

For the formation of the transparent electrode, the metal square structures on the mesa regions must then be preferentially removed without damaging the embedded metal-mesh structures. As schematically described in [Figure](#)

1b, we introduce two types of ASD methods based on the **synergic combination of solvent-induced adhesion control and mechanical stimuli**. As shown in [Figure 1c–e](#), a well-defined nanomesh structure can be formed only by the combined effects of solvent-assisted interfacial delamination and appropriate mechanical stimulus, which will be discussed in detail based on experimental observations.

First, we show how the solvent influences the interface between PUA and the deposited metal. In order to choose an appropriate solvent for the **swelling of PUA**, the *in situ* swelling ratio of the PUA thin film was measured under three solvent vapors—deionized (DI) water, ethanol, and **heptane**. As shown in [Figure 2a](#), the PUA substrate was swollen significantly (more than 16%) by ethanol over 16% (note that a swelling ratio beyond 16% could not be measured because of delamination of PUA from the Si wafer due to significant volume expansion), while the thickness of PUA immersed in DI water and heptane molecules increased by a maximum of 4 and 2%, respectively. The PUA swelling phenomenon by ethanol can also be seen in [Figure S1](#) in the [Supporting Information](#), where it is seen that the PUA/PET substrate bent downward because the upper PUA layer swelled significantly, whereas PET did not. [Figure 2c](#) shows the *in situ* optical microscope images of the Ag-deposited



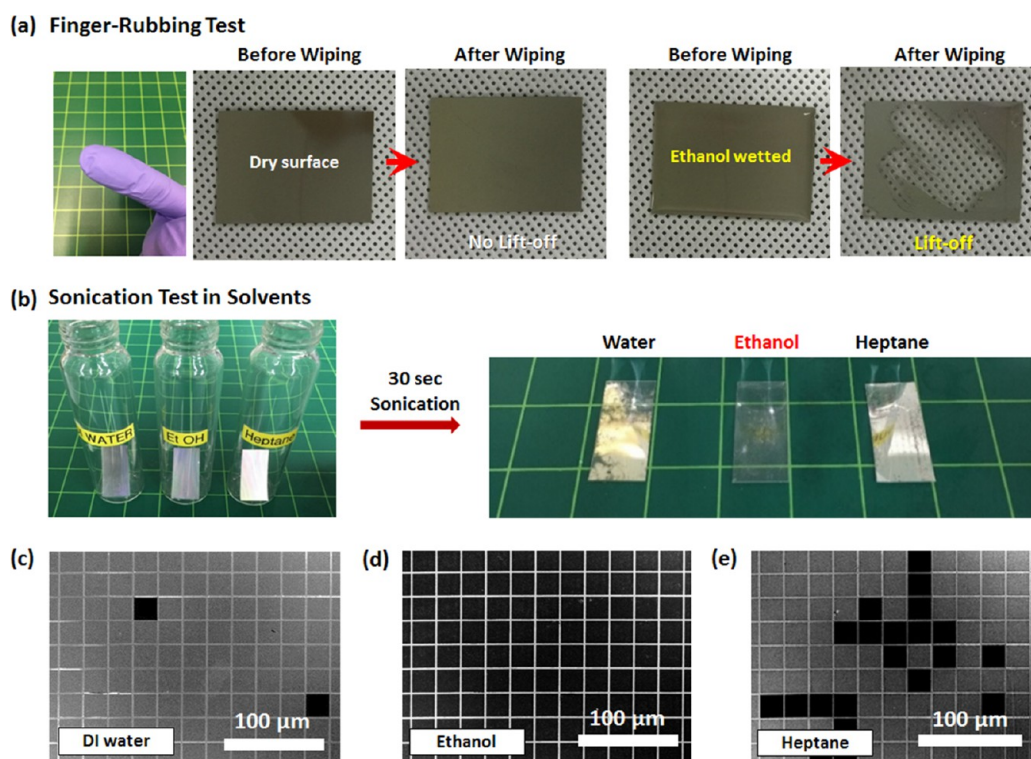


**Figure 4.** Effect of solvent on the reliable and uniform ASD of Ag squares. (a) Wiping test using a finger on the surface of the Ag/PUA replica. Ag was peeled off only when ethanol was dropped on the surface. (b) Ultrasonication treatment in three different solvents (water, ethanol, and heptane). After 30 s treatment, ASD of Ag occurred only in ethanol. (c–e) SEM images of the samples after 30 s sonication in (c) water, (d) ethanol, and (e) heptane. Highly uniform ASD was achieved using ethanol.

PUA replica with increasing ethanol soaking time. Before swelling of the PUA substrate (time sequence = 0), all the areas appear bright, suggesting that the beam paths of incident and reflected beams are parallel and that there is no noticeable deformation of the PUA/metal interface.

After immersion in the chosen solvent (ethanol), however, a small fraction of the square metal plate areas began to rapidly changed to a dark color (Figure 2c, time sequence = 1–3, 20 s for each sequence), which soon spread over almost the entire area (sequence = 4). This can be attributed to the fact that ethanol, as a good solvent, can swell the volume of PUA and deform the flat interface between PUA and the metal. Moreover, the solvent molecules incorporated at the interface can significantly weaken the adhesion force between the silver films and the PUA surface, as we demonstrated in a previous study.<sup>31</sup> As schematically shown in Figure 2b, these combined effects by solvent incorporation would tilt the metal square plates from a surface-parallel orientation, resulting in off-axis reflection from the square metal plates and causing a reduction of brightness because the reflected beam from the misaligned Ag squares is not collected by the charge-coupled device camera. Similarly, as shown in Figure S2 in the Supporting Information, the reflection of a cell phone camera lens on the surface of the Ag-deposited PUA replica disappeared upon immersion in ethanol. This suggests significant roughening of the surface by the tilting of the Ag plates, which is contrasted by the relatively clear reflection image of the sample immersed in water (=poor solvent). However, if the sample immersed in the ethanol bath is removed from the solvent and is dried, the optical reflection behavior returned to the original state before immersion in the solvent, as presented in Figure 2d and Movie S1 in the Supporting Information in detail. These observations

imply that the silver squares even under the ethanol environment were not completely detached from the PUA, and therefore, an additional stimulus is needed to break the interfacial adhesion.

Therefore, we employed two types of mechanical stimuli that can effectively and permanently detach the square plate structures from the mesa regions. First, we applied a soft rubbing technique using a paper wiper. An ethanol-soaked paper wiper was rubbed on the Ag-deposited PUA replica. With rubbing of the surface with a moderate pressure, the deposited silver films on the mesa were easily removed and washed away (as presented in Figure 3a–f and Movie S2 in the Supporting Information). In contrast, the metal structures were not peeled off when a dry paper was used (Figure 4a), confirming the essential role of the solvent for the delamination of the metal. Figure 3g,h presents scanning electron microscopy (SEM) images of well-defined embedded metal-mesh electrodes obtained by the wiping ASD process. The electrical and optical characteristics of these electrodes will be discussed in detail. Moreover, this solvent-assisted wiping ASD process can also be applied to other geometries such as line patterns and also to different mesh patterns with a smaller line width of 150 nm, as shown in Figure S3 in the Supporting Information, indicating its versatility as a convenient pattern transfer technique.

An alternative way of providing a mechanical stimulus with better simplicity and shorter processing time is the use of **ultrasonication treatment**. As shown in Figure S4 in the Supporting Information, SEM images of Si master molds with the same mesh width of 950 nm and different heights of 450, 800, and 1200 nm were used to prepare PUA replica samples. A Ag thin film with a thickness of 300 nm was deposited on the replica. For the ASD process, a Ag-deposited PUA replica was

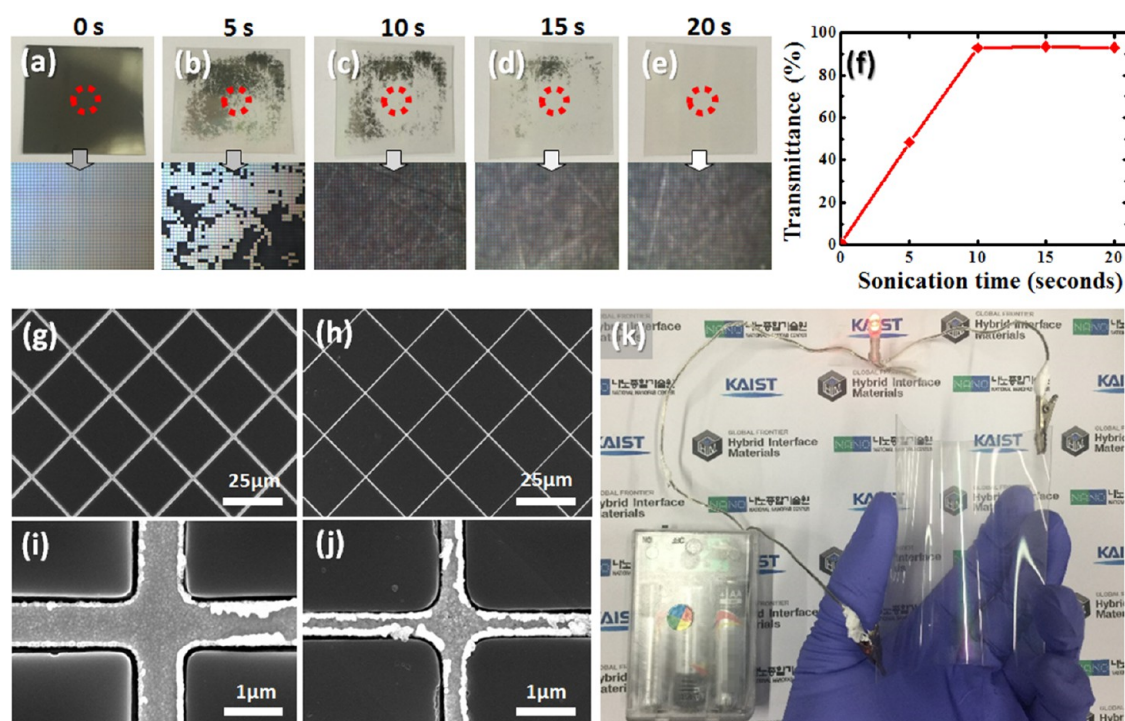


**Figure 5.** Fabrication of a metal-mesh electrode by an ultrasonication ASD process. (a–e) Optical images of Ag/PUA replica/PET with increasing ultrasonication treatment time in ethanol. (f) Change of optical transmittance at a wavelength of 550 nm as a function of treatment time. (g–j) SEM images of metal-mesh electrodes prepared using the ultrasonication ASD process. (k) Photograph of the flexible transparent electrode; used with permission, the background is the logos of KAIST, NNFC, and HIM.

immersed in an ethanol bath placed in an ultrasonicator. The yield of ultrasonication ASD was highly dependent on the solvent. As presented in Figure 4b–e, other solvents such as water and heptane did not assist the ASD of Ag, confirming again the important role of the solvent in the delamination of the metal from the PUA surface.

Appropriate sonication time was dependent on the geometrical parameters of the Si master mold and the replicated PUA. As shown in the bottom of Figure S4 in the Supporting Information, the necessary sonication time decreased with an increase of height. In the cases of 450 and 800 nm depths of the mesh trenches, silver films still remained on the mesa after 270 and 90 s of sonication time, respectively. However, for the PUA replica with a 1200 nm depth, there were no remaining silver plates on the mesa and no broken parts of the embedded mesh pattern after 60 s of sonication time. This is because, for deeper trenches, the thickness of the films deposited at the sidewalls is smaller due to the so-called shadowing effect. Therefore, the mesh patterns and square plates are more easily disconnected during the ASD process. These results indicate that highly uniform ASD can be implemented by optimizing the geometrical parameters of the replicas. Figure 5a–f depicts the transmittance changes as a function of the sonication treatment time, showing the completion of ASD after 20 s. SEM images of well-defined electrode patterns fabricated with the sonication lift-off process are shown in Figure 5g–j. A macroscopic sample with a large area of 10 cm × 10 cm was prepared, and good electrical conductance and transmittance were confirmed, as shown in Figure 5k.

For transparent electrodes, it is important to obtain both higher transmittance and low sheet resistance. Figure 6a plots the total transmittance ( $T$ , reference = PET) in the visible range of our Ag nanomesh transparent electrode formed by the

wiping ASD process and the sonication ASD process, showing high optical transmittance values over 90%. In Figure 6b,  $T$  at the wavelength of 550 nm and the sheet resistance ( $R_s$ ) values are displayed in comparison with the results of previous studies in the literature (metal mesh,<sup>2,9,15,16,19,28</sup> hybrid,<sup>17,32–34</sup> and metal wire-based<sup>35–37</sup> electrodes). For example, a 400 nm thick Ag nanomesh electrode with 900 and 400 nm line widths showed  $T = 94\%$  and  $R_s = 1.43 \Omega \text{ sq}^{-1}$  and  $T = 97\%$  and  $R_s = 2.86 \Omega \text{ sq}^{-1}$ , respectively, indicating that a wider mesh width provides lower sheet resistance while compromising transmittance. However, when the height of the Ag electrode was increased from 400 to 800 nm without changing the line width (900 nm), the same transmittance of 94% and a much lower  $R_s$  of  $0.43 \Omega \text{ sq}^{-1}$  were achieved, showing the independent controllability of the sheet resistance without sacrificing transmittance (also see Figure S5, Supporting Information). This can be attributed to the almost constant opening ratio of the metal-mesh structure despite the substantial height change of the structures. These results demonstrate the advantage of the metal-nanomesh electrode compared to the Ag nanowire electrode, where there is a strong trade-off between transparency and conductivity. This is because metal nanowires should be sparsely distributed for high transparency, which inevitably accompanies a significant increase of sheet resistance.<sup>14</sup>

For a more quantitative comparison of performances as a transparent electrode, figure-of-merit (FoM) values were calculated. In reference to previous studies, we used the following equation, where  $\sigma_{\text{dc}}$  is the electrical conductance and  $\sigma_{\text{opt}}$  is the optical conductance.<sup>19</sup>



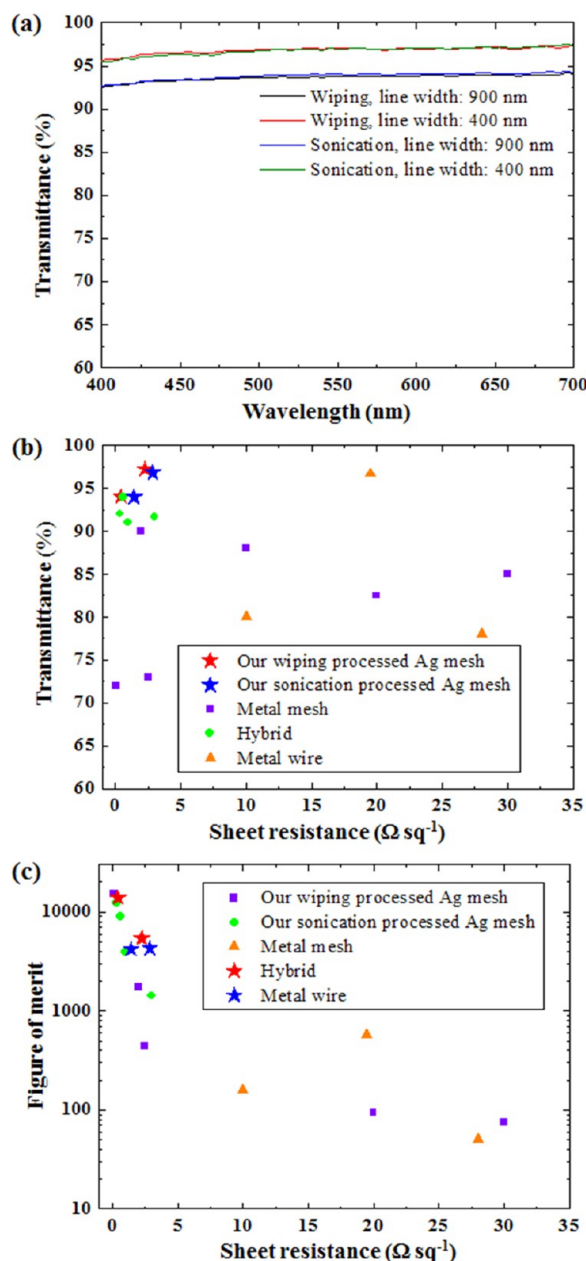


Figure 6. Performances of the flexible transparent electrode. (a) Total transmittance in the visible range depending on nanomesh dimensions. (b) Transmittance (at wavelength = 550 nm) versus sheet resistance data of the metal-nanomesh electrode in comparison with previous studies (metal mesh,<sup>2,9,15,16,19,28</sup> hybrid,<sup>17,32–34</sup> and metal wire<sup>35–37</sup> types; highest values for each research paper were included). (c) Comparison of the figure of merit (FoM) values.

$$\text{FoM} = \frac{\sigma_{\text{dc}}}{\sigma_{\text{opt}}} = \frac{188.5}{R_s \left( \frac{1}{\sqrt{T}} - 1 \right)} \quad (1)$$

Hybrid-type and metal-mesh-type electrodes demonstrated outstanding performance in comparison with that of metal-wire-based electrodes.<sup>17,19</sup> In our work, we achieved a high FoM of  $1.33 \times 10^4$  with a high transmittance of 94%. Thus far, the highest FoM value reported in the literature is about  $1.58 \times 10^4$  ( $T = 73\%$ ,  $R_s = 0.07 \Omega \text{ sq}^{-1}$ ), which was obtained by photolithography, electrodeposition of  $2 \mu\text{m}$  thick metal, and an imprint transfer process (Figure 6c).<sup>19</sup> However, this low

transmittance range is far below the transmittance ( $>85\%$ ) of practical transparent electrodes. For a comparable transmittance of 94%, the FoM of the metal-mesh electrode in the previous study decreased to  $\sim 9.8 \times 10^3$ . The spectra of total transmittance, direct transmittance, and calculated haze values were measured for the various nanomesh electrodes fabricated in this study (Figure S6, Supporting Information).

Figure 7a provides comparative bending stability test results for the embedded metal-mesh flexible transparent electrodes and a commercial ITO/PET electrode. As already known, the resistance of the commercial ITO/PET electrode increased rapidly according to the bending cycles with a bending radius of 5 mm, and failure occurred before 50 cycles. In contrast, the low sheet resistance of our metal-mesh electrode was maintained for more than 1000 cycles, confirming outstanding bending stability without any noticeable change of the transmittance at the wavelength of 550 nm (Figure 7a and Figure S7 in the Supporting Information). This can be attributed to the structural advantage of the embedded geometry, and this result is consistent with previous studies.<sup>19,38</sup>

We also performed a chemical stability test in different solvent environments such as pure water,  $0.1 \text{ mol L}^{-1}$  salt water (with  $\sim 20$  times higher  $\text{Cl}^-$  concentration than human sweat), ethanol (a swelling solvent for PUA replica), and isopropyl alcohol (IPA, a widely used cleaning solvent), as shown in Figure 7b–d. For the immersion time of 36 h, no noticeable changes of electrical resistance and optical transmittance were observed, confirming the outstanding stability of the transparent electrode, where three sides of the structure are passivated by the polymer.

The flexible transparent electrode in this study showed one of the highest performance levels reported thus far in terms of durability, transparency, and electrical conductivity. For example, this flexible nanomesh electrode can be directly applied to a high-performance transparent heater.<sup>19,39</sup> After contact electrodes were formed on both sides of the nanomesh sample, direct current (DC) voltages were swept (Figure 8a). The infrared (IR) image presented in Figure 8a shows uniformly generated heat at 3 V. The measured temperatures on the Ag mesh sample ( $R_s = 1.26 \Omega \text{ sq}^{-1}$ ) and a commercial ITO-coated substrate ( $R_s = 8.16 \Omega \text{ sq}^{-1}$ ) as a function of the applied voltage are provided in Figure 8b. This graph shows a much faster temperature increase for the nanomesh electrode, which can be attributed to the several times smaller resistance of the nanomesh electrode. To further demonstrate the potential of the Ag mesh film as an efficient defroster, a defrosting test was conducted. After a sample was placed in a refrigerator for 15 min, it was taken out and exposed to ambient conditions to form a thick frost layer over the entire surface. The frost was completely removed within 10 s with an applied voltage of 3 V, as shown in Figure 8c. Also, Figure 8d demonstrates that water droplets formed on the heater were entirely evaporated within 120 s of heater operation. In addition, the flexible transparent electrodes can be used as high-performance optoelectronics and flexible electronic devices. By taking full advantage of the flexible transparent electrodes, we demonstrated a highly transparent touch panel. A four-wire resistive touch panel was configured using a nanomesh electrode/PET sample and an ITO-coated PET substrate. The structure of the fabricated touch panel, which has a small insulating gap (distance = 700 nm) between the upper and lower transparent electrode, is schematically shown in Figure 8e. It should be noted that the small gap is naturally formed by

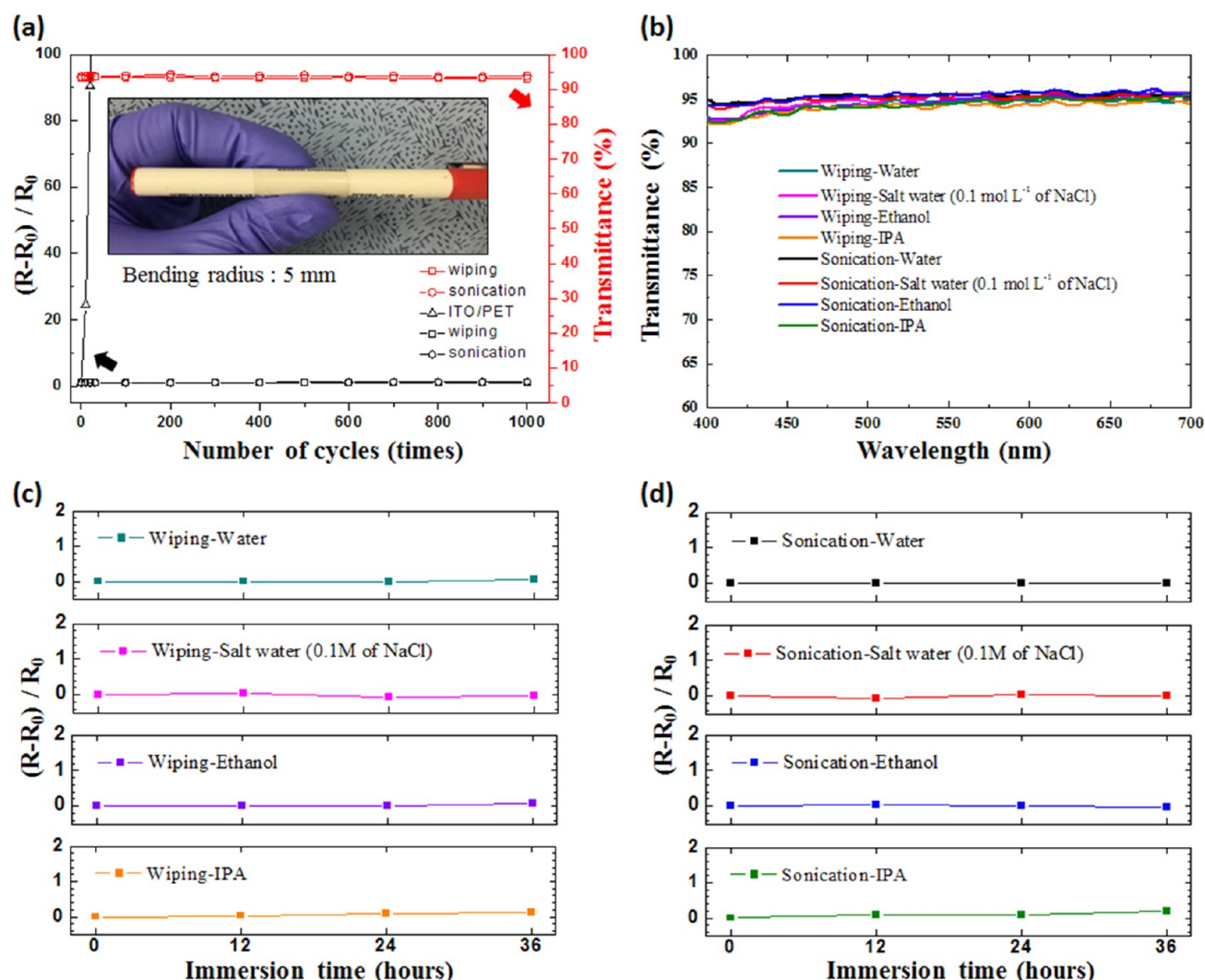


**Figure 7.** Reliability of the flexible transparent electrode. (a) Bending cycle test results of ITO/PET and fabricated embedded-type metal-mesh flexible transparent electrodes. The bending radius is 5 mm. (b–d) Investigation of chemical stability in water, salt water, ethanol, and isopropyl alcohol. (b) Transmittance of each sample after 36 h. (c,d) Change of the normalized sheet resistance ( $R$ ) as a function of immersion time (0–36 h). Samples were prepared by (c) soft-wiping-based ASD and (d) ultrasonication-based ASD.  $R_0$  indicates the  $R$  value of the samples before bending.

optimizing the deposited Ag film thickness for reliable area-selective lift-off, as demonstrated above. The application of local pressure deforms the upper nanomesh electrode, which allows electrical conduction between the two conductive layers. The overall configuration of the touch panel device with high transmittance is presented in Figure 8f. Successful touch recognition and handwriting using a stylus on the touch panel are demonstrated in Figure 8g and Movie S3 in the Supporting Information. These examples again confirm the long-range electrical connectivity and excellent reliability of the nanomesh electrode fabricated in this study.

## CONCLUSION

In summary, we demonstrated a highly facile fabrication strategy for embedded-type metal-mesh flexible transparent electrodes on the basis of a solvent-assisted adhesion weakening mechanism and the application of controlled mechanical stimuli. This method does not require the repetition of complex photolithography or etching steps and is potentially suitable for roll-to-roll fabrication. When specific solvent

molecules (e.g., ethanol for PUA replication polymer) were injected into the interface between Ag and PUA, the molecules effectively weakened the adhesion strength between the Ag film and the PUA substrate based on an interfacial screening effect and caused partial delamination resulting from the volume expansion of the PUA replica, which was monitored and confirmed by *in situ* optical microscopy imaging. Permanent, area-selective lift-off of the Ag square structure from the PUA replica was completed by an additional mechanical stimulus such as mechanical wiping or ultrasonication treatment, resulting in well-defined metal-nanomesh structures. The fabricated nanomesh transparent electrodes showed outstanding optoelectronic performances with an extremely low sheet resistance ( $0.43 \, \Omega \, \text{sq}^{-1}$ ) and a high optical transmittance (94%). We also demonstrated tuning of the sheet resistance without compromising the transmittance by controlling the aspect ratio of the mesh structure. Also, the repeated bending cycle test and chemical durability test results confirm the reliability of the nanomesh electrode. The demonstration of transparent and flexible heater and touch panel devices



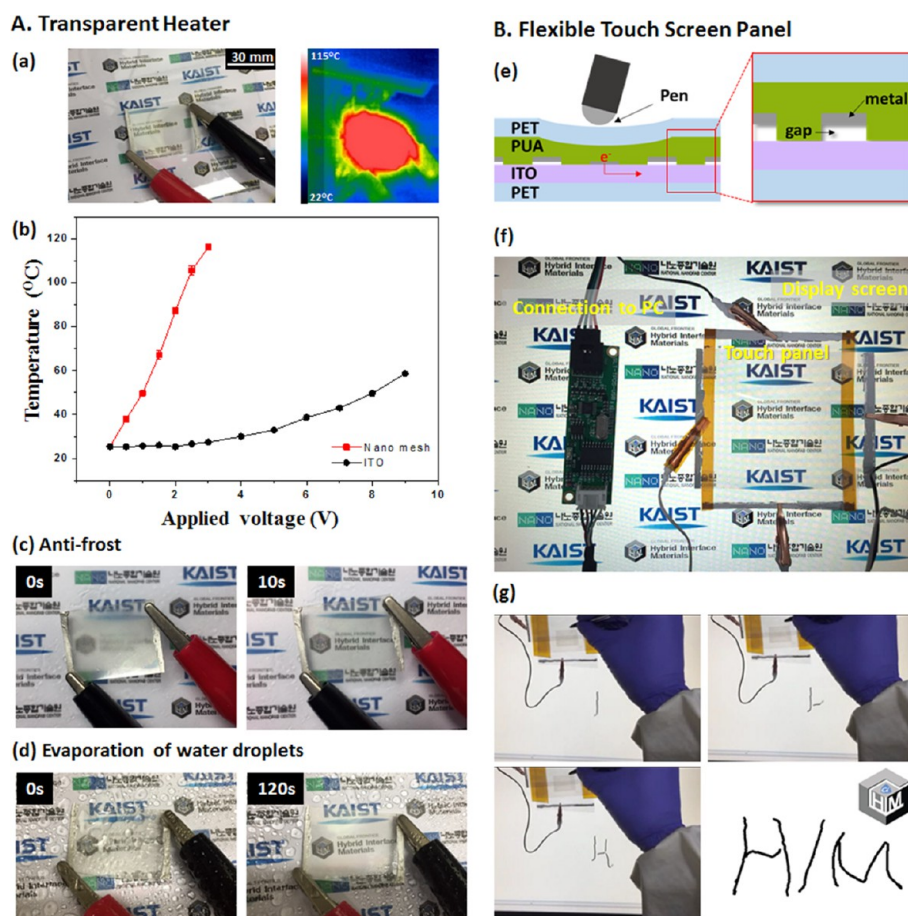


**Figure 8.** Applications of the flexible transparent electrode. (A) Transparent heating device. (a) Ordinary photograph (left) and thermal image taken with an infrared camera (right) of the transparent heater operated at an applied voltage of 3 V. (b) Comparison of temperature increase for two types of transparent conductor (Ag nanomesh and ITO) as a function of applied voltage. (c) Defrost test results before and after application of voltage (3 V). (d) Evaporation of water droplets on the backside of the heater (applied voltage = 3 V). (B) Flexible touch screen panel. (e) Schematic of the cross-section structure of the resistive-type touch panel constructed with the nanomesh electrode and ITO electrode. (f) Configuration of the touch panel device. An image from the LCD monitor is clearly visible through the highly transparent touch panel. (g) Demonstration of letter-writing operation; used with permission, the background is the logo of HIM. Also see [Movie S3](#) in the Supporting Information. The background of panels (a,c,d,f) is the logos of KAIST, NNFC, and HIM, used with permission.

prepared using the nanomesh electrode suggests its promising potential applicability. The outstanding simplicity of this ASD fabrication process can substantially reduce processing cost and complexity and lower the barrier to the commercialization of flexible transparent electrodes. Moreover, our findings may suggest an alternative route for low-cost and high-yield production of a variety of other device components such as light emitters, light-trapping or outcoupling structures, polarizers, and so on, which are based on well-defined micro/nanoscale functional elements.

## EXPERIMENTAL SECTION

**Silicon Master Mold Preparation.** Si master molds were fabricated using KrF photolithography followed by reactive ion etching. A positive photoresist (PR, Dongjin Semichem Co. Ltd.) with a thickness of 1  $\mu\text{m}$  was spin-coated on 8 in. Si wafers. The PR film was then exposed using a KrF scanner (Nikon, NRS-S203B), followed by developing using a developer solution (tetramethylammonium hydroxide, Dongjin Semichem Co. Ltd.) The PR patterns were used as an etch mask to pattern the Si wafer surface by reactive ion etching (gas,  $\text{CF}_4$  for etching,  $\text{C}_4\text{F}_8$  for wall passivation; working pressure, 10 mTorr; plasma power, 165 W).

**Fabrication of PUA Replica Substrate.** For the fabrication of the PUA replica, PUA (MINS-311RM, MINS-ERM, Minuta Technology

Co. Ltd.) was drop-casted on the hexamethyldisilazane-treated silicon master mold and covered by PET film. The PUA/PET substrate was cured by a UV light (lamp power = 400 W, time = 10 min, peak wavelength = 365 nm) and was detached from the Si master mold.

**Deposition of Metal Films.** Silver was deposited through physical vapor deposition onto the PUA substrate with thermal evaporation. The distance between the PUA substrate and the silver source was about 30 cm. The deposition rate of silver was  $5 \text{ \AA s}^{-1}$ .

**Sheet Resistance and Transmittance Measurement.** Sheet resistance was measured by a Hall measurement system (HMS-3000, ECOPIA Co., Ltd.). Direct transmittance was measured by UV-vis spectroscopy (Optizen POP, Mecasys Co., Ltd.) using bare PET as a reference. Total transmittance was measured by a UV/vis/NIR spectrophotometer (SolidSpec-3700, Shimadzu Scientific Instruments) equipped with an integrating sphere.

**SEM Characterization.** For the characterization of the samples, a field emission SEM (Hitachi S-4800) was used with an acceleration voltage of 10 kV, and a working distance of 5 mm was used. Before observation, samples were coated with osmium.

**In Situ Measurement of Swelling Ratio of PUA Films.** The *in situ* variation of the PUA (MINS-ERM and MINS-311RM) thickness under the various solvent vapors (DI water, ethanol, heptane) was measured using a reflectometer (F20-UV, Filmetrics Inc.) with a measurement wavelength range of 350–1100 nm.

**Device Fabrication and Characterization.** For the transparent heater, a DC power supply (Keithley 2280S-32-6) was used to induce Joule heating, and the thermal images were captured in real-time by an infrared camera (LW-AAA, Seek Thermal). The touch panel was connected to a computer using an interface controller (4-wire resistive-type controller, Hantouch).

## ASSOCIATED CONTENT

### Supporting Information

The Supporting Information is available free of charge on the ACS Publications website at DOI: 10.1021/acsnano.7b00229.

Supplementary Figures S1–S7 (PDF)

Movie S1 (AVI)

Movie S2 (AVI)

Movie S3 (AVI)

## AUTHOR INFORMATION

### Corresponding Authors

\*E-mail: kwhokim@pusan.ac.kr.

\*E-mail: ysjung@kaist.ac.kr.

### ORCID

Yeon Sik Jung: 0000-0002-7709-8347

### Author Contributions

<sup>†</sup>S.Y. and H.J.H. contributed equally to this work.

### Notes

The authors declare no competing financial interest.

## ACKNOWLEDGMENTS

This research was supported by Global Frontier Program through the Global Frontier Hybrid Interface Materials (GFHIM) of the National Research Foundation of Korea (NRF) funded by the Ministry of Science, ICT & Future Planning (2013M3A6B1078874). This work was also supported by Open Innovation Lab Project from National Nanofab Center (NNFC).

## REFERENCES

- (1) Kang, M. G.; Xu, T.; Park, H. J.; Luo, X. G.; Guo, L. J. Efficiency Enhancement of Organic Solar Cells Using Transparent Plasmonic Ag Nanowire Electrodes. *Adv. Mater.* **2010**, *22*, 4378–4383.
- (2) Han, B.; Pei, K.; Huang, Y. L.; Zhang, X. J.; Rong, Q. K.; Lin, Q. G.; Guo, Y. F.; Sun, T. Y.; Guo, C. F.; Carnahan, D.; Giersig, M.; Wang, Y.; Gao, J. W.; Ren, Z. F.; Kempa, K. Uniform Self-Forming Metallic Network as a High-Performance Transparent Conductive Electrode. *Adv. Mater.* **2014**, *26*, 873–877.
- (3) Lee, J.; Lee, P.; Lee, H. B.; Hong, S.; Lee, I.; Yeo, J.; Lee, S. S.; Kim, T. S.; Lee, D.; Ko, S. H. Room-Temperature Nanosoldering of a Very Long Metal Nanowire Network by Conducting-Polymer-Assisted Joining for a Flexible Touch-Panel Application. *Adv. Funct. Mater.* **2013**, *23*, 4171–4176.
- (4) Bae, S.; Kim, H.; Lee, Y.; Xu, X. F.; Park, J. S.; Zheng, Y.; Balakrishnan, J.; Lei, T.; Kim, H. R.; Song, Y. I.; Kim, Y. J.; Kim, K. S.; Ozyilmaz, B.; Ahn, J. H.; Hong, B. H.; Iijima, S. Roll-to-Roll Production of 30-Inch Graphene Films for Transparent Electrodes. *Nat. Nanotechnol.* **2010**, *5*, 574–578.
- (5) Hagerott, M.; Jeon, H.; Nurmikko, A. V.; Xie, W.; Grillo, D. C.; Kobayashi, M.; Gunshor, R. L. Indium Tin Oxide as Transparent Electrode Material for ZnSe-Based Blue Quantum-Well Light Emitters. *Appl. Phys. Lett.* **1992**, *60*, 2825–2827.
- (6) Schmidt, H.; Flugge, H.; Winkler, T.; Bulow, T.; Riedl, T.; Kowalsky, W. Efficient Semitransparent Inverted Organic Solar Cells with Indium Tin Oxide Top Electrode. *Appl. Phys. Lett.* **2009**, *94*, 243302.
- (7) Tahar, R. B. H.; Ban, T.; Ohya, Y.; Takahashi, Y. Tin Doped Indium Oxide Thin Films: Electrical Properties. *J. Appl. Phys.* **1998**, *83*, 2631–2645.
- (8) Garnett, E. C.; Cai, W.; Cha, J. J.; Mahmood, F.; Connor, S. T.; Greyson Christoforo, M.; Cui, Y.; McGehee, M. D.; Brongersma, M. L. Self-Limited Plasmonic Welding of Silver Nanowire Junctions. *Nat. Mater.* **2012**, *11*, 241–249.
- (9) Wu, H.; Kong, D.; Ruan, Z.; Hsu, P.-C.; Wang, S.; Yu, Z.; Carney, T. J.; Hu, L.; Fan, S.; Cui, Y. A Transparent Electrode Based on a Metal Nanotrough Network. *Nat. Nanotechnol.* **2013**, *8*, 421–425.
- (10) Im, H. G.; Jung, S. H.; Jin, J.; Lee, D.; Lee, J.; Lee, D.; Lee, J. Y.; Kim, I. D.; Bae, B. S. Flexible Transparent Conducting Hybrid Film Using a Surface-Embedded Copper Nanowire Network: A Highly Oxidation-Resistant Copper Nanowire Electrode for Flexible Optoelectronics. *ACS Nano* **2014**, *8*, 10973–10979.
- (11) Wu, Z.; Chen, Z.; Du, X.; Logan, J. M.; Sippel, J.; Nikolou, M.; Kamaras, K.; Reynolds, J. R.; Tanner, D. B.; Hebard, A. F. Transparent, Conductive Carbon Nanotube Films. *Science* **2004**, *305*, 1273–1276.
- (12) Lipomi, D. J.; Vosgueritchian, M.; Tee, B. C. K.; Hellstrom, S. L.; Lee, J. A.; Fox, C. H.; Bao, Z. Skin-Like Pressure and Strain Sensors Based on Transparent Elastic Films of Carbon Nanotubes. *Nat. Nanotechnol.* **2011**, *6*, 788–792.
- (13) Vosgueritchian, M.; Lipomi, D. J.; Bao, Z. Highly Conductive and Transparent PEDOT: PSS Films With a Fluorosurfactant for Stretchable and Flexible Transparent Electrodes. *Adv. Funct. Mater.* **2012**, *22*, 421–428.
- (14) Lee, J. Y.; Connor, S. T.; Cui, Y.; Peumans, P. Solution-Processed Metal Nanowire Mesh Transparent Electrodes. *Nano Lett.* **2008**, *8*, 689–692.
- (15) Hong, S.; Yeo, J.; Kim, G.; Kim, D.; Lee, H.; Kwon, J.; Lee, H.; Lee, P.; Ko, S. H. Nonvacuum, Maskless Fabrication of a Flexible Metal Grid Transparent Conductor by Low-Temperature Selective Laser Sintering of Nanoparticle Ink. *ACS Nano* **2013**, *7*, 5024–5031.
- (16) Guo, C. F.; Sun, T. Y.; Liu, Q. H.; Suo, Z. G.; Ren, Z. F. Highly Stretchable and Transparent Nanomesh Electrodes Made by Grain Boundary Lithography. *Nat. Commun.* **2014**, *5*, 3121.
- (17) Hsu, P. C.; Wang, S.; Wu, H.; Narasimhan, V. K.; Kong, D. S.; Lee, H. R.; Cui, Y. Performance Enhancement of Metal Nanowire Transparent Conducting Electrodes by Mesoscale Metal Wires. *Nat. Commun.* **2013**, *4*, 2522.
- (18) Sciacca, B.; van de Groep, J.; Polman, A.; Garnett, E. C. Solution-Grown Silver Nanowire Ordered Arrays as Transparent Electrodes. *Adv. Mater.* **2016**, *28*, 905–909.
- (19) Khan, A.; Lee, S.; Jang, T.; Xiong, Z.; Zhang, C. P.; Tang, J. Y.; Guo, L. J.; Li, W. D. High-Performance Flexible Transparent Electrode with an Embedded Metal Mesh Fabricated by Cost-Effective Solution Process. *Small* **2016**, *12*, 3021–3030.
- (20) De, S.; Higgins, T. M.; Lyons, P. E.; Doherty, E. M.; Nirmalraj, P. N.; Blau, W. J.; Boland, J. J.; Coleman, J. N. Silver Nanowire Networks as Flexible, Transparent, Conducting Films: Extremely High DC to Optical Conductivity Ratios. *ACS Nano* **2009**, *3*, 1767–1774.
- (21) Hu, L.; Kim, H. S.; Lee, J.-Y.; Peumans, P.; Cui, Y. Scalable Coating and Properties of Transparent, Flexible, Silver Nanowire Electrodes. *ACS Nano* **2010**, *4*, 2955–2963.
- (22) Lee, S. J.; Kim, Y. H.; Kim, J. K.; Baik, H.; Park, J. H.; Lee, J.; Nam, J.; Park, J. H.; Lee, T. W.; Yi, G. R.; Cho, J. H. A Roll-to-Roll Welding Process for Planarized Silver Nanowire Electrodes. *Nanoscale* **2014**, *6*, 11828–11834.
- (23) Lee, J. Y.; Connor, S. T.; Cui, Y.; Peumans, P. Semitransparent Organic Photovoltaic Cells with Laminated Top Electrode. *Nano Lett.* **2010**, *10*, 1276–1279.
- (24) Lee, D.; Youn, D. Y.; Luo, Z.; Kim, I. D. Highly Flexible Transparent Electrodes Using a Silver Nanowires-Embedded Colorless Polyimide Film via Chemical Modification. *RSC Adv.* **2016**, *6*, 30331–30336.
- (25) Preston, C.; Xu, Y. L.; Han, X. G.; Munday, J. N.; Hu, L. B. Optical Haze of Transparent and Conductive Silver Nanowire Films. *Nano Res.* **2013**, *6*, 461–468.



- (26) Kim, H. J.; Lee, S. H.; Lee, J.; Lee, E. S.; Choi, J. H.; Jung, J. H.; Jung, J. Y.; Choi, D. G. High-Durable AgNi Nanomesh Film for a Transparent Conducting Electrode. *Small* **2014**, *10*, 3767–3774.
- (27) Yang, G. H.; Liu, B.; Cheng, K.; Du, Z. L. Modulation of Optical Transmittance and Conductivity by the Period, Linewidth and Height of Au Square Mesh Electrodes. *Opt. Express* **2015**, *23*, A62–A70.
- (28) Schneider, J.; Rohner, P.; Thureja, D.; Schmid, M.; Galliker, P.; Poulikakos, D. Electrohydrodynamic NanoDrip Printing of High Aspect Ratio Metal Grid Transparent Electrodes. *Adv. Funct. Mater.* **2016**, *26*, 833–840.
- (29) Cho, H.; Kim, J.; Park, H.; Bang, J. W.; Hyun, M. S.; Bae, Y.; Ha, L.; Kim, D. Y.; Kang, S. M.; Park, T. J.; Seo, S.; Choi, M.; Suh, K. Y. Replication of Flexible Polymer Membranes with Geometry-Controlable Nano-Apertures via a Hierarchical Mould-Based Dewetting. *Nat. Commun.* **2014**, *5*, 3137.
- (30) Choi, S. J.; Kim, H. N.; Bae, W. G.; Suh, K. Y. Modulus- and Surface Energy-Tunable Ultraviolet-Curable Polyurethane Acrylate: Properties and Applications. *J. Mater. Chem.* **2011**, *21*, 14325–14335.
- (31) Jeong, J. W.; Yang, S. R.; Hur, Y. H.; Kim, S. W.; Baek, K. M.; Yim, S.; Jang, H. I.; Park, J. H.; Lee, S. Y.; Park, C. O.; Jung, Y. S. High-Resolution Nanotransfer Printing Applicable to Diverse Surfaces via Interface-Targeted Adhesion Switching. *Nat. Commun.* **2014**, *5*, 5387.
- (32) An, B. W.; Hyun, B. G.; Kim, S.-Y.; Kim, M.; Lee, M.-S.; Lee, K.; Koo, J. B.; Chu, H. Y.; Bae, B.-S.; Park, J.-U. Stretchable and Transparent Electrodes Using Hybrid Structures of Graphene–Metal Nanotrough Networks with High Performances and Ultimate Uniformity. *Nano Lett.* **2014**, *14*, 6322–6328.
- (33) Bao, W.; Wan, J.; Han, X.; Cai, X.; Zhu, H.; Kim, D.; Ma, D.; Xu, Y.; Munday, J. N.; Drew, H. D. Approaching the Limits of Transparency and Conductivity in Graphitic Materials Through Lithium Intercalation. *Nat. Commun.* **2014**, *5*, 4224.
- (34) Gao, T. C.; Li, Z. T.; Huang, P. S.; Shenoy, G. J.; Parobek, D.; Tan, S. S.; Lee, J. K.; Liu, H. T.; Leu, P. W. Hierarchical Graphene/Metal Grid Structures for Stable, Flexible Transparent Conductors. *ACS Nano* **2015**, *9*, 5440–5446.
- (35) Yin, Z.; Song, S. K.; You, D. J.; Ko, Y.; Cho, S.; Yoo, J.; Park, S. Y.; Piao, Y.; Chang, S. T.; Kim, Y. S. Novel Synthesis, Coating, and Networking of Curved Copper Nanowires for Flexible Transparent Conductive Electrodes. *Small* **2015**, *11*, 4576–4583.
- (36) Kang, S.; Kim, T.; Cho, S.; Lee, Y.; Choe, A.; Walker, B.; Ko, S.-J.; Kim, J. Y.; Ko, H. Capillary Printing of Highly Aligned Silver Nanowire Transparent Electrodes for High-Performance Optoelectronic Devices. *Nano Lett.* **2015**, *15*, 7933–7942.
- (37) Garnett, E. C.; Cai, W.; Cha, J. J.; Mahmood, F.; Connor, S. T.; Christoforo, M. G.; Cui, Y.; McGehee, M. D.; Brongersma, M. L. Self-Limited Plasmonic Welding of Silver Nanowire Junctions. *Nat. Mater.* **2012**, *11*, 241–249.
- (38) Choi, H. J.; Choo, S.; Jung, P. H.; Shin, J. H.; Kim, Y. D.; Lee, H. Uniformly Embedded Silver Nanomesh as Highly Bendable Transparent Conducting Electrode. *Nanotechnology* **2015**, *26*, 055305.
- (39) Kim, H.-J.; Kim, Y.; Jeong, J.-H.; Choi, J.-H.; Lee, J.; Choi, D.-G. A Cupronickel-Based Micromesh Film for Use as a High-Performance and Low-Voltage Transparent Heater. *J. Mater. Chem. A* **2015**, *3*, 16621–16626.